WEAR AND MECHANICAL PROPERTIES OF IN SITU A356/5%TiB$_2$ COMPOSITE SYNTHESIS BY COOLING SLOPE TECHNIQUE

Sujeet Kumar Gautam and Sudip Kumar Samanta
Foundry Group, CSIR-Central Mechanical Engineering Research Institute, Durgapur 713209, India

Manab Mallik
Metallurgy and Material Engineering, National Institute of Technology, Durgapur 713209, India

Himadri Roy
NDT &Metallurgy Group, CSIR-Central Mechanical Engineering Research Institute, Durgapur 713209, India

Aditya Kumar Lohar
Surface Engineering and Tribology, CSIR-Central Mechanical Engineering Research Institute, Durgapur 713209, India

Abstract

The main aim of this study is to understand the microstructure characterization, mechanical properties and wear behavior of in situ processed A356/5%TiB$_2$ rheocast metal matrix composite. This investigation deals with an aluminum-based in situ composite wherein the reinforcement, TiB$_2$, was synthesized in the molten alloy via reaction of salts between K$_2$TiF$_6$ and KBF$_4$. The paper shall cover a few aspects of this new generation of composites, such as the development of in situ composite and distribution pattern (grain structure), size and number of TiB$_2$ in cast ingot of A356 aluminum alloy with 5% TiB$_2$. The obtained results revealed that cast condition of A356/ TiB$_2$ composite, primary phase of aluminum alloy and eutectic Si phase are normally in the refined shape and

TiB$_2$ particles are mostly in the hexagonal or near spherical shape, with the size ranging from size 1 to 5 μm uniformly distributed throughout the microstructure. It has been found that the mechanical properties of rheocast composite material are enhanced with addition of TiB$_2$ particles. The wear rate of the composites improves significantly with the TiB$_2$ content. Analysis of the worn surfaces suggests that adhesion and ploughing are the predominant wear mechanisms.

Keywords: metal matrix composite, A356 Al alloy, TiB$_2$, mechanical properties, wear behavior

Introduction

Aluminum metal matrix composites (MMCs) can offer improved mechanical properties over their base alloys.[1–3] Ceramic-reinforced composites are fabricated by incorporating ceramic reinforcement materials like aluminum oxide (Al$_2$O$_3$), titanium carbide (TiC), silicon carbide (SiC) and titanium boride (TiB$_2$). Titanium boride (TiB$_2$) is one of the best reinforcements for aluminum alloy because it

has the highest tensile strength, compression strength, and toughness.

Several processes for fabricating aluminum-based composites have been developed, including liquid casting, solid state, and in situ techniques. Liquid casting is considered the most common process among them because it is simple. It is more economical than other manufacturing processes and is suitable for large-scale production, which makes it an ideal choice for manufacturers.[4,5] However, the development of composite materials using the liquid casting method comes with some disadvantages. Due to the lack of wettability, it is difficult for the ceramic particles to

be mixed into the matrix. In addition, several defects, including porosity formation, interfacially reactive reactions, and non-uniform reinforcement distribution, arise.[6] When using the liquid casting method, there is always a difference in density between the reinforcement and the surrounding matrix. As a result, if the particles sink or float, they cause a non-uniform distribution of reinforcement. As a result, due to poor particle dispersion, agglomeration takes place, which results in the formation of high porosities in the composite.[7,8] Various techniques have been reported to improve the wetting properties between the particle and matrix, including the addition of surfactants,[9] polymers,[10] and nanoparticles.[11] An alternative way to improve wettability is to heat the alloy to a semisolid state.[6–8,12–14] Semisolid metal casting is an alternative method for casting metals. It is called rheocasting.

Semisolid metal processing (SSM) is an economical way to manufacture lightweight metals. It has superior metallurgical and mechanical characteristics compared to the traditional casting technique.[15] Refining the grain size of the slurries can help reduce defects such as voids, craters, pores, and others. Refinement may be achieved by processing in a mesh region.[15]

The essential need of SSM is the semisolid slurry generation.[16,17] There are number of processes to generate the semisolid slurry like shear cooling roll (SCR), gas-induced semisolid (GISS), gas bubbling, magneto hydrodynamic (MHD) stirring, mechanical rotational barrel (MRB), etc.[18,19] Kiuchi and Sugiyama[20] developed a new process based on mechanical stirring process (shear cooling roll). In this method, slurry forms in the gap between a rotating roll and a stationary cooling 'shoe'. As the metal solidifies in the gap, a continuous slurry stream is produced by the shearing and cooling action of the rotating roll. From a practical perspective, these mechanical processes have several disadvantages, the most important being the erosion of the stirrer, melt contamination by debris and oxides, gas entrapment and low productivity.[21–24] The employment of rotational forces during solidification is an alternative approach which is more attractive because it is non-intrusive and the stirring intensity (and direction) may be easily modulated at will. In gas-induced semisolid (GISS) and gas bubbling methods, inert gas was injected through a porous graphite diffuser into the molten metal. The agitated action created by flowing inert gas in the molten metal.

Thus, the development of in situ composite material requires suitable slurry generation system so as to meet the requirement of slurry on demand. Cooling slope technique to produce semisolid slurry is the simplest process and having less controlling parameters. At the same time, cooling slope technique meets the slurry on demand as it is one of the requirements of the casting process. In this work cooling slope technique has been chosen. There are several key factors, i.e., slope angle, slope length, pouring temperature, etc., which are directly affect the quality of semisolid slurry.

In the present study, an aluminum titanium diboride (Al/TiB$_2$) in situ composite was prepared by using the cooling slope technique. Wear behavior and mechanical properties are an important consideration when designing an aluminum-based in situ TiB$_2$ composite by rheocasting. There are various works that consider the mechanical properties of particular composites and compare them with others.[25,26] The majority of the works are built with in situ stir cast Al-TiB$_2$ composites. As the content of TiB$_2$ increases, so does the wear resistance of the material. In addition, the consequences of in situ reaction and grain refinement on the wear properties of aluminum-based metal matrix composite have been investigated. It has been reported that how wear trends vary in high temperatures is also being investigated.[27]

According to the review of literature, A356 composite reinforced with TiB$_2$ has already been successfully fabricated; however, the effect of the cooling slope casting technique on the microstructure, mechanical, and tribological behavior of the composite has yet to be thoroughly investigated. Therefore, the main focus of this research is investigating the effect of the cooling slope process on the tribological behavior and mechanical properties of an A356/5wt%TiB$_2$ composite material. A356-TiB$_2$ composite was fabricated via the cooling slope technique. The wear test was carried out in a dry sliding environment with varying applied loads at constant sliding distance and speed. Optical and SEM with EDS are utilized to evaluate the microstructure of rheocast composite material and also analyze the worn surface and debris of rheocast composite in order to identify potential wear mechanisms. The effect of in situ-generated TiB$_2$ particles in composite is also investigated thoroughly and associated to mechanical properties.

Experimental Work

Chemical composition of as-received A356 aluminum alloy is mentioned in Table 1. As-received A356 Al alloy (202.94 gm) was melted inside silicon carbide crucible in the electric furnace, at 750 °C. The Al-10% Mg master alloy of 6 gm was added to the molten metal to compensate for the Mg loss and degassed. The molten metal was held in isothermal condition at 20 min for fully homogenization. The reinforcement salts, K$_2$TiF$_6$ (34.63 gm) and KBF$_4$ (36.52 gm) were fully blended and wrapped into aluminum foil and preheated at a temperature 250 °C for 1 h in order to remove the humidity. After the fully homogenization of melt, preheated salts were added in molten metal. The molten metal was stirred by graphite rod every 10 min, so that all the salts could be completely dissolved into the alloy. After that aluminum went into the exothermal

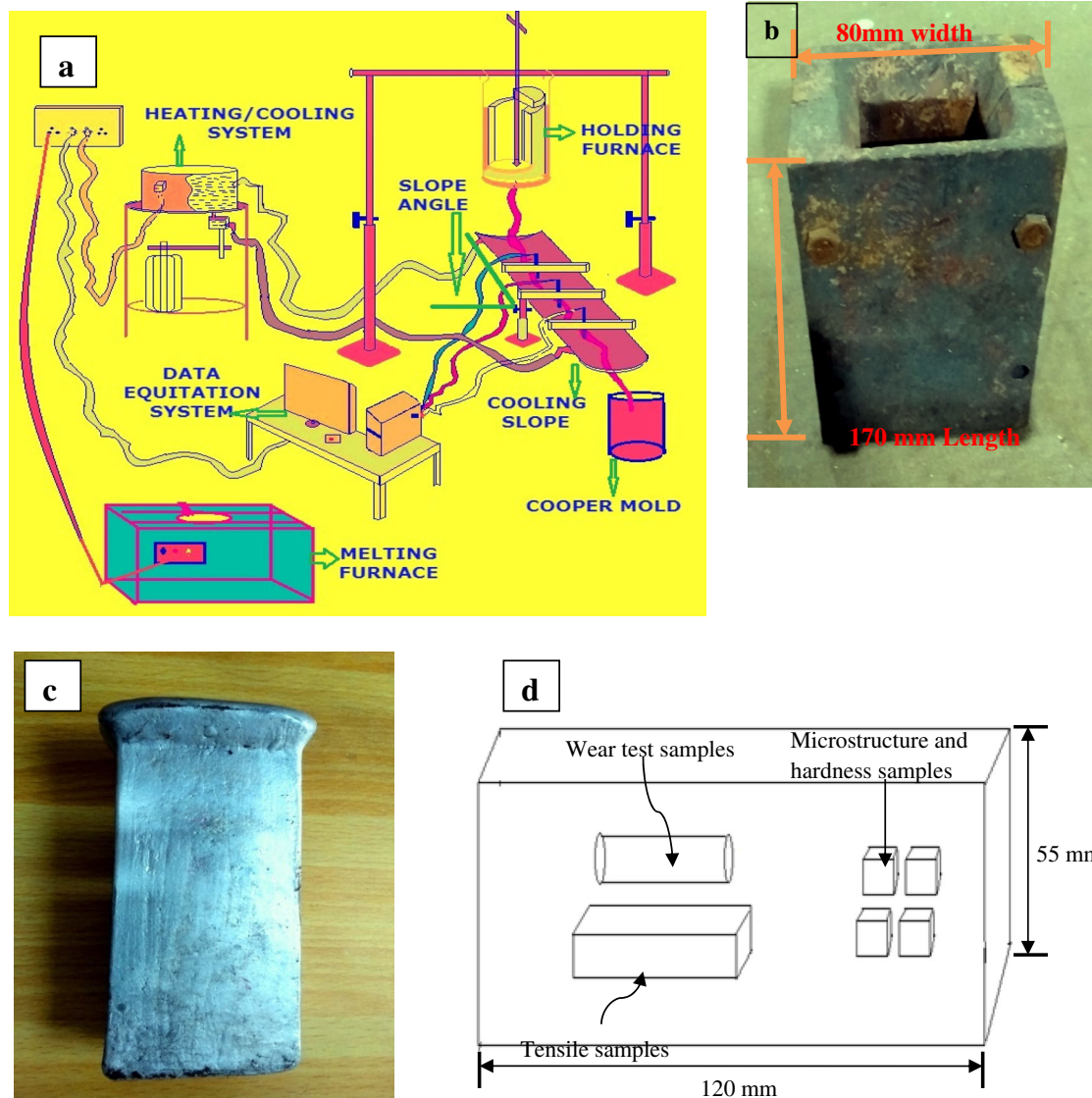| Alloy	Composition (wt %)							
	Si	Cu	Mg	Ti	Fe	Mn	Zn	Al
A356	6.5	<0.001	0.318	0.01	0.20	0.076	0.083	Balance

Figure 1. (a) Schematic diagram of cooling slope technique, (b) dimension of copper mold (170 mm × 80 mm), (c) image of cast and (d) various samples of cast product.

reaction with the slag and produced petite sparkles. When the aluminum reacted, titanium diboride was formed which entered the liquid metal. In order to avoid overheating the system, the furnace was shut down during this reaction. The molten metal was agitated constantly to ensure that there was adequate contact between the melt and slag. This process was continued until no longer evidence of sparking. This showed that the reaction was complete. When the reactions were completed, the slag was removed from the crucible. Then, the molten metal was poured into holding furnace, which was placed at the top of cooling slope plate as shown in Figure 1a. The molten metal was flow over cooling slope plate for semisolid slurry generation. The authors in their earlier work[28] have already reported the optimized process parameters of cooling slope technique for A356 Al alloy. Cooling slope plate was coated with boron nitride to prevention of sticking of liquid melt. At the exit of the cooling slope, the slurry was collected in the preheated copper mold (at 200 °C) and cooled down at ambient temperature. The dimension of copper mold is

length 170 mm and width 80 mm as shown in Figure 1b. The experiment was repeated three times to get three rectangular bar with width 60 mm and length 120 mm (as shown in Figure 1c). Also for the purpose of comparison, gravity casting (GC) of A356 Al alloy was carried out using the same mold and with the same superheat. Finally, samples were extracted from rectangular bar as shown in Figure 1d.

Characterization

The specimen dimensions of 10 mm x 10 mm x 10 mm for metallography were extracted from various casts as shown in Figure 1d. The surface of the samples was prepared by polishing on SiC papers of grades 180–2000 grits until the scratches of the previous stage completely disappeared. This was followed by polishing on lapping clothes attached to a rotating disk and smeared with 1 μm diamond paste until a scratch free surface finish was obtained. The specimens were etched with Keller's reagent for a period of about ∼10 s to delineate the grain boundaries. The microstructural investigation of the alloy and composite was done using a scanning electron microscope (SEM) coupled with energy-dispersive X-ray spectroscopy (EDS). Compositional analysis and X-ray mapping were carried out using the EDX microanalysis. X-ray diffraction (XRD) was used to identify the crystal structure of the constituent phases.

The specimens were fabricated from various cast materials (as shown in Figure 1d) to evaluate their mechanical properties. The dimension of the tensile specimen is shown in Figure 2. According to the ASTM standard E-8M, from each experiment, three flat tensile specimens were machined from solidified billets. Tensile tests were carried out using a 50 kN Universal Tensile Testing Machine at 0.5 mm/sec displacement rate. After tensile testing, the fractured surfaces were characterized by field emission scanning electron microscopy (SEM) for fractographic analysis. Hardness measurements were taken on the metallographically prepared surface of specimens using a Vicker's hardness tester operating at a load of 5 kgf allowing a dwell time for indentation of 15 seconds. At least ten indentations were taken for each specimen, and the average values were reported.

The extent of grain size of various cast samples is measured by following Eqn. 1.

$$S.F = \left(\frac{4\pi A_\alpha}{P_\alpha^2}\right) \qquad \text{Eqn. 1}$$

where S.F, A_α and P_α shows area, shape factor (particle size) and perimeter of the primary phase and eutectic phases of cast samples, respectively.

Density of various cast samples was calculated by Archimedes principle. Theoretical density of various cast samples was determined as per following Eqn. 2.
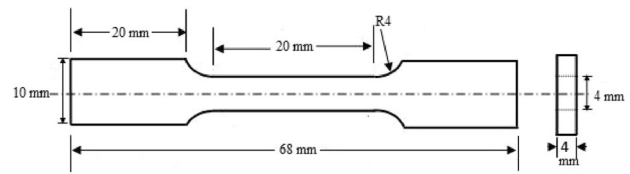

Figure 2. Dimensions of tensile test specimen.

$$\rho_{th} = \frac{1}{\frac{W_m}{\rho_m} + \frac{W_f}{\rho_m}} \qquad \text{Eqn. 2}$$

In the above equation, ρ_{th} is representing the theoretical density of various cast specimens. W_m and W_f are weight fractions of matrix and reinforcement, respectively. Whereas ρ_m and ρ_f are densities of matrix and reinforcement, respectively. Average percentage porosity was calculated using the actual and theoretical density as per following Eqn. 3.

$$\%\text{Porosity} = \frac{\rho_{th} - \rho_{ac}}{\rho_{th}} \times 100 \qquad \text{Eqn. 3}$$

where ρ_{th} and ρ_{ac} are the theoretical and actual density of samples, respectively.

Evaluation of Dry Sliding Wear Properties

Dry sliding wear tests of cast materials were conducted on a pin-on-disk wear-testing machine (DUCOM, India). This experimental work was based on the ASTM G99-05 (ASTM, 1992) standard. Cylindrical specimens were fabricated from various cast materials to evaluate their wear properties as shown in Figure 1d. The dimensions of cylindrical specimens of cast samples are 25 mm in length and 5 mm in diameter and are to be used as pins. These cylindrical pins were tested by subjecting them to sliding wear tests under loads of 10-30 Newton against a disk of steel at room temperature. Every test was performed by moving the disk at a constant speed of 300 rpm for a distance of 5652 meters. The process of sliding involves sliding a disk (with a radius of 100 mm) against a pin. The counter disk is an EN 31 steel disk (hardness = 60 HRC, HV 695). The hardness of the disk is almost 10 times higher than the hardness of the as-cast A356 alloy. The counter disk has not worn during the test. To maintain uniform surface roughness, all tests were performed using the same track diameter (100 mm). After each test, the surface of the disk was cleaned with acetone. The wear surfaces of specimens were characterized by SEM.

Results and Discussion

Microstructural Characterization

The composition of the A356 aluminum alloy indicates that it is in accordance with the standard composition of A356. The presence of these elements is also confirmed by X-ray diffraction analysis as shown in Figure 3. In order to determine the formation of intermetallics and distribution of reinforcement particle within the base matrix, it is conducted. Aluminum, silicon and magnesium peaks were appeared in the gravity cast sample of A356 alloy. A TiB_2 peak was observed in the rheocast composite sample. It reveals the existence and distribution of reinforcement and other phases in greater concentration. The presence of the weak intermetallic phase (Mg_2Si, which was confirmed by EDS) has an effect on the properties of this composite material. It has been reported by researchers that they act as preferred fracture sites and their propagation.[29]

Figure 4a shows the grain morphology of primary phase of CG sample of A356 aluminum alloy, which has a long dendritic structure surrounded by elongated and needle-shaped eutectic phases of Si (which are also confirmed by EDS analyses). The presence of these eutectic phases is also reported through EDS analysis. The presence of large size Si- and Mg-rich intermetallic induces stress concentration, which deteriorates the mechanical properties.[30]

It is evident from Figure 5a, the primary phase of aluminum alloy is seen to be equiaxed and rosette apart from refinement in intermetallic phases, which appear small but well distributed without the needle-like structures. The SEM micrographs along with EDS analysis of the rheocast composite a sample are shown in Figure 5b. The SEM study at high magnification revealed the uniformly distributed of reinforcement particles in the matrix and also the presence of a nearly globular shape of a primary phase of composite material along with an intermetallic phase, which was confirmed by EDS analysis (as shown in Figure 5c). As shown in Figure 7b, most of the TiB_2 particles are mostly in the hexagonal or near spherical shapes, with the sizes ranging 1 to 5 μm uniformly distributed throughout the microstructure as shown in Figure 5d.

The change in microstructure into the nearly globular and rosette morphology of the primary phase and refinement of eutectic phases in rheocast composite samples is due to shear forces acting on the solidifying melt along the cooling slope. As the liquid metal flows over the surface of cooling slope, it easily loses its thermal energy and the temperature drops below its melting point. It favors the nucleation and formation of primary aluminum phase. These nucleated particles are later captured by the flowing liquid and are then collected at the bottom of slope before they fully grow into larger crystals.[31] The values of grain size of primary phase of a-Al aluminum and eutectic phase
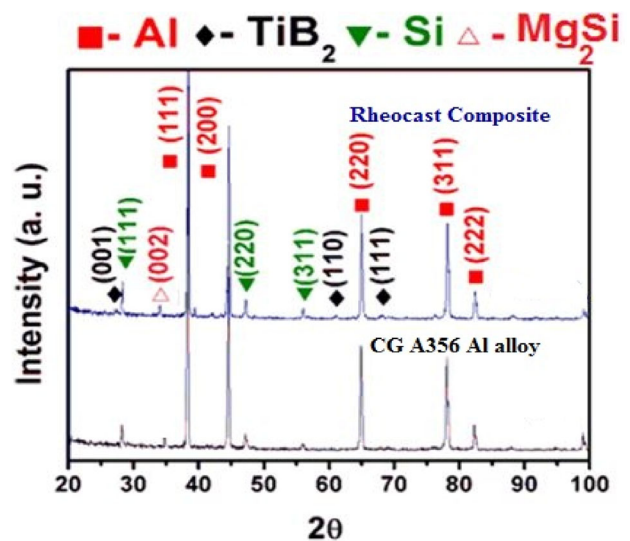

Figure 3. XRD pattern showing the peaks of phases present in CG cast A356 alloy and rheocast composite.

of rheocast composite is found to be lower compared to the gravity cast sample. The grain sizes of primary phase of α-Al and eutectic phase of rheocast composite sample are 55 μm and 33 μm, respectively. The grain sizes of primary phase of a-Al and eutectic phase gravity cast sample are 91 μm and 88 μm, respectively. The finer particle size plays a key role for mechanical properties of rheocast composite process.[32–34] Extent of porosities in the rheocast composite sample is found to be lower compared to gravity cast sample. Density of the composites has been measured by the Archimedes principle. The theoretical densities of CG A356 alloy and rheocast composite are 2.67 g/cm³ and 2.73 g/cm³, respectively. The densities of the rheocast composite, measured by the rule of mixtures using theoretical density of A356 alloy and TiB_2 particles, are 2.67 g/cm³ and 4.52 g/cm³, respectively. The measured densities of CG A356 alloy and rheocast composite are 2.43 g/cm³ and 2.52 g/cm³, respectively. The relative densities of CG A356 alloy and rheocast composite are 91% and 92%, respectively. Therefore, the porosity present in the CG A356 alloy and rheocast composite is 9% and 8%, respectively.

Mechanical Properties

Figure 6 depicts the variations in hardness values of CG A356 aluminum alloy and developed rheoast composite specimens. The observed graph indicates that the rheocast composite has the highest value of hardness (74.50 HV), followed by A356 aluminum (64 HV). With the addition of TiB_2 particles, a prominent increase in the hardness of the composite can be observed. It has been scientifically proven that when a hard reinforcement is integrated within a ductile matrix, the hardness of the composite material increases. Additionally, the refinement of grains was
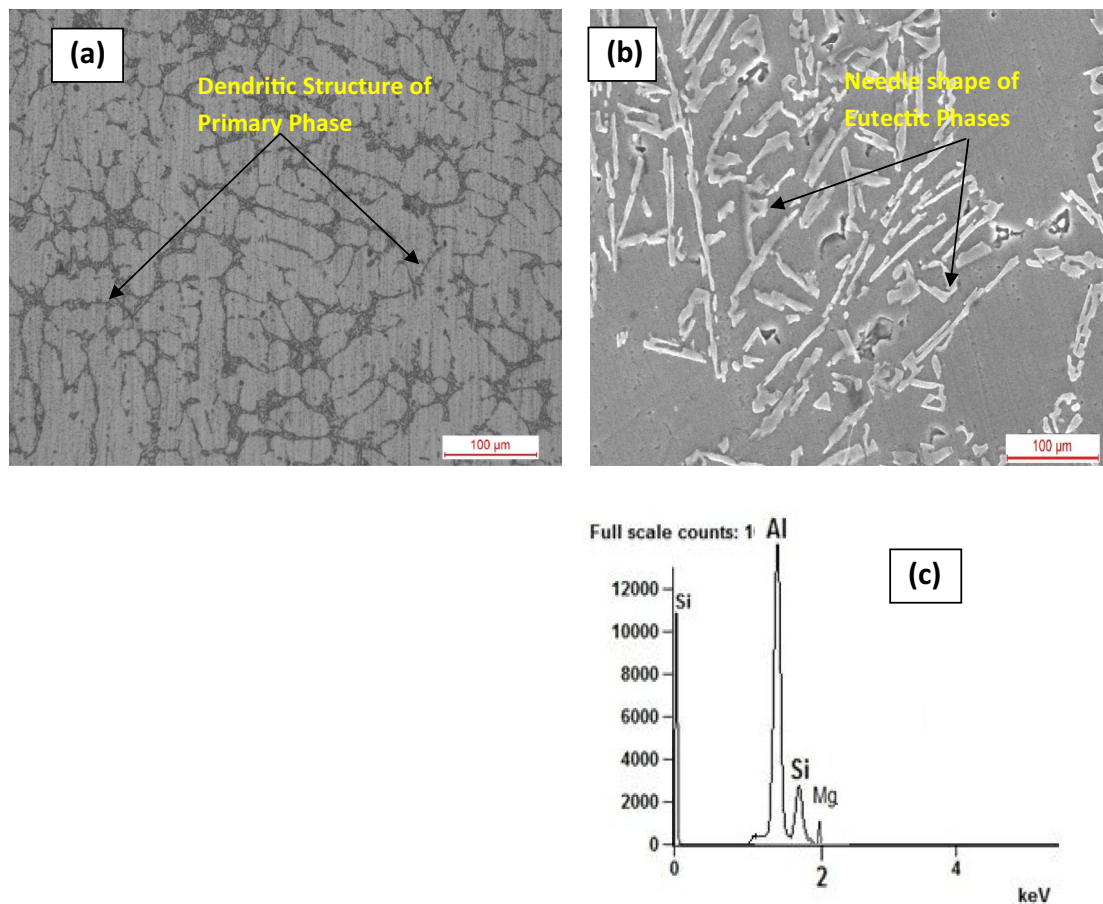
Figure 4. *(a) Optical microscope microstructures, (b) SEM micrograph and (c) EDS of CG A356 alloy.*

achieved by the processing of composite material in the semisolid state condition. The hardness is also governed by the semisolid metal processing. Several researchers have observed similar behavior when incorporating titanium diboride into any of the metallic matrix composites.

To determine the suitability of a material for automotive and structural applications, it is very important to measure the tensile properties. The tensile properties of various cast materials were estimated from a tensile bar. The average values of rheocast composite obtained are as follows: Young modulus: 77, Yield strength: 190, Tensile Strength: 225 and Elongation 7 %, respectively (as shown in Table 2), which have the higher values compared to CG A356 aluminum alloy (Young modulus 70, Yield strength 170, Tensile Strength 194 MPa, and Elongation 9 %). The results indicate that rheocast composite exhibits better mechanical properties compared to CG A365 aluminum alloy. Microstructural study of rheocast composite shows that globular alpha Al grains are surrounded by TiB_2 particles. These TiB_2 particles act as grain growth inhibitors and refine the microstructure. Fine grain structure and uniform distribution of TiB_2 particles along grain boundaries are the main reasons for strengthening of rheocast composites. Hard ceramic TiB_2 particles restrict dislocation movement and enhance work

hardening. The possible presence of dendritic morphology in the primary phase of aluminum alloy and elongated brittle phases (intermetallics) and porosity limits the strength in CG A356 aluminum alloy sample.

Table 2 represents the tensile properties, e.g., Young's modulus (E), yield strength (σy) at 0.2% strain, tensile strength (σ TS) and EL% (Elongation) of various cast materials.

In order to examine the micromechanism of fracture, the broken tensile specimens from each material were inspected under electron microscope. The observed fractograph of the CG of A356 aluminum alloy exhibits essentially transgranular facets with secondarily fracture running across the brittle eutectic colonies. A cellular region is an area of the fracture surface of an alloy which has been identified by microscopy as having a particular microstructure. The fracture surface is not showing true dimples as shown by Figure 7a. The incorporation of titanium diboride particles into the aluminum matrix leads to small, shallow depressions and ductile failure modes at the fractured surface.[35] Few large and deep dimples can be seen in Figure 7b. Shallow dimples are normally observed to distribute more uniformly in the fractography. Most of
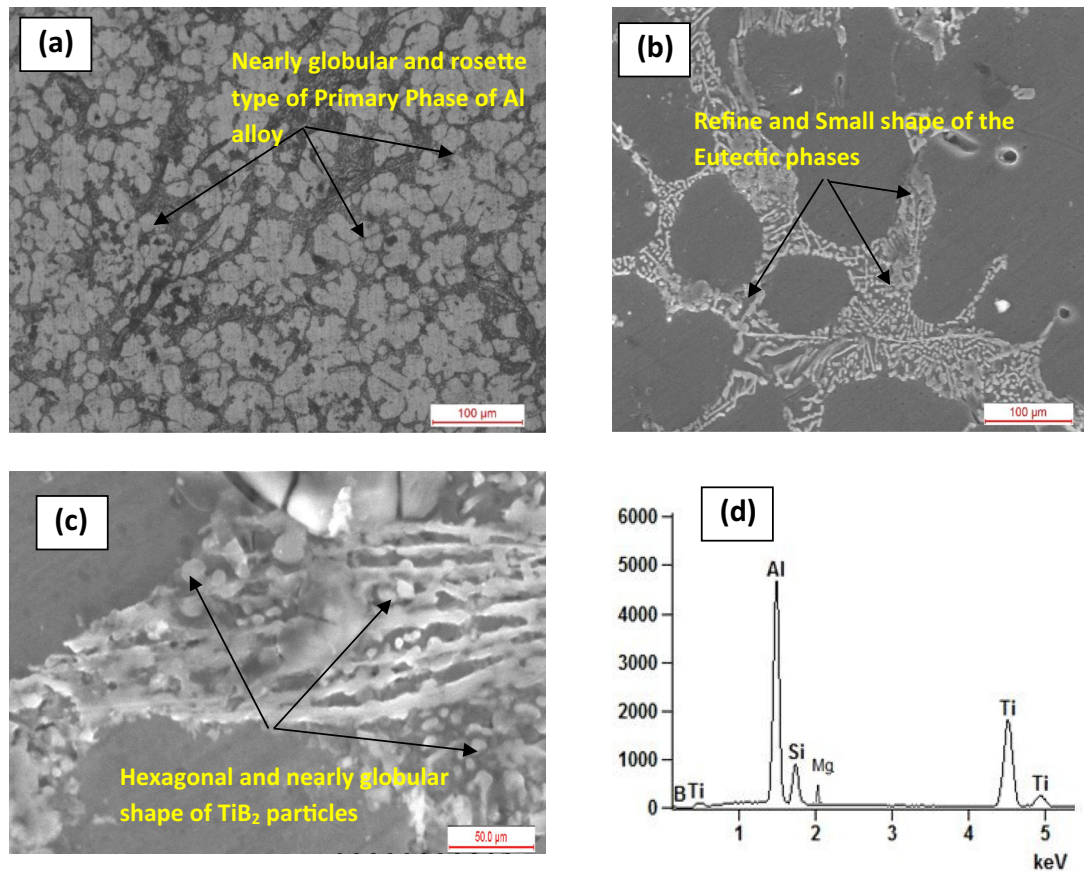
Figure 5. *(a) Optical microscope microstructures, (b) SEM micrograph, (c) SEM micrograph of at high magnification and (d) EDS of rheocast composite.*
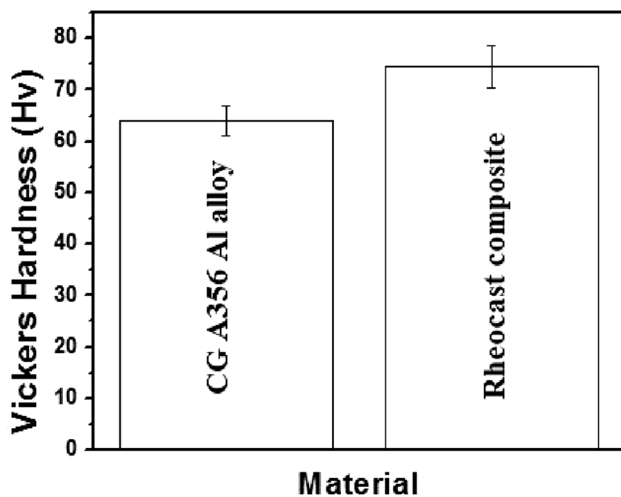

Figure 6. *Bar charts showing: Vickers hardness values of CG A356 alloy and rheocast composite.*

the dimple sizes are smaller than 5 μm, which indicates that the particles are very fine. Some dimples contain TiB_2 particles while others show signs of debonding.[36] The fracture patterns of these specimens (rheocast condition) indicate the ductile mode of failure as evidenced by the formation of more shallow and finer dimples than in the CG A356 alloy condition.

Table 2. Tensile Properties of CG A356 Al Alloy and Rheocast Composite

Material	Young's modulus (E, GPa)	Yield strength (σ_y, MPa)	Tensile strength (σ_{UTS}, MPa)	El (%)
CG A356 alloy	70	170±5	194±6	9
Rheocast composite	77	190±3	225±5	7

Wear Behavior of CG A356 Alloy and Rheocast Composite

This investigation reports the wear behavior of CG A356 Al alloy and rheocast Al-based metal matrix composite reinforced with in situ TiB_2 particles. The wear behavior of various cast materials is investigated under various normal loads. As cast sample wear behavior is interpreted in terms of worn surfaces and debris formed during the steady state dry sliding wear. In order to understand the wear behavior of cast samples, it is necessary to perform chemical and microstructural analyses of debris and worn surfaces formed by the wear test. During dry sliding wear, the
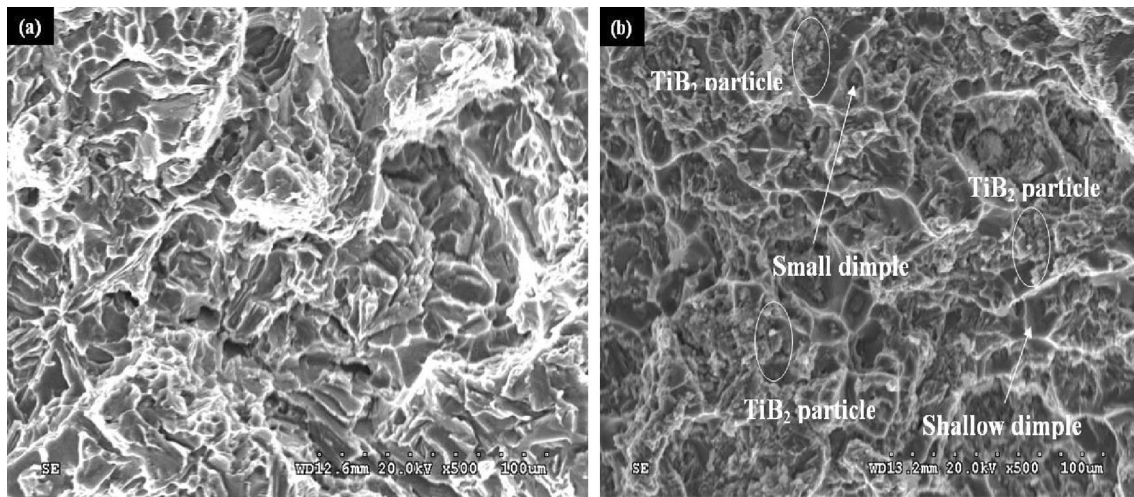
Figure 7. SEM images of tensile fracture surfaces (a) CG A356 alloy and (b) rheocast composite.
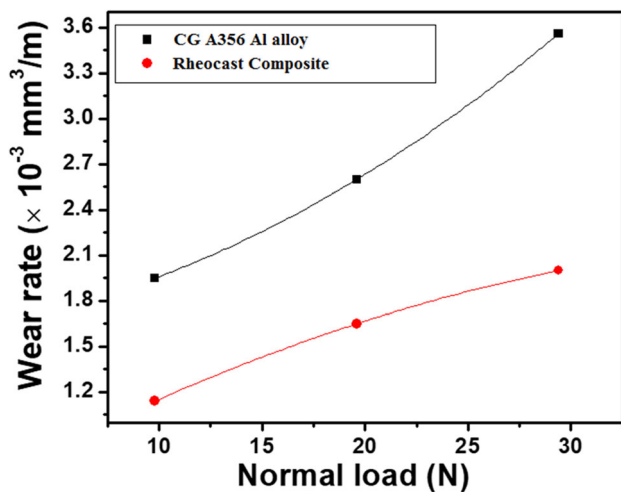

Figure 8. Plot showing wear rate of CG A356 Al alloy and rheocast composite at different loads.

relative motion between two solid surfaces causes the transfer of material between the contacting surfaces through solid-state welding, or localized bonding.[37]

The pin-on-disk wear-testing machine operated under the normal load of 9.8–29.4 N has been employed to study the dry sliding wear characteristics of CG A356 alloy and rheocast composite. The wear rates have been estimated and analyzed.

The wear of the titanium-based reinforced composite (Al/TiB$_2$) was compared with the wear of CG aluminum alloy (A356) for all applied load cases. Figure 8 shows that the wear rate of the alloy and composite increases steadily as the normal load increases. As shown in the graph, at lower loads, the wear resistance is relatively low. With an increase in load, the wear resistance decreases. Wear resistance is the reciprocal of wear rate, which means that if wear rate increases, wear resistance decreases. Titanium diboride reinforcement improves the wear resistance of

A356 aluminum alloy. In this study, adding titanium diboride particles to an alloy (A356) resulted in a combination of grain refinement and modification, which led to better wear resistance. Wear study suggests that there is a significant improvement in the wear resistance of the composites due to the presence of TiB$_2$ particles. Fine microstructure and uniform distribution of TiB$_2$ particles enhance work hardening of rheocast composite during wear. As a result surface hardness of the rheocast composite increases during wear and reduces wear rate.

Wear Surfaces of CG A356 Alloy and Rheocast Composite

Figure 9a and b shows the characteristic of the worn surfaces of CG A356 alloy and rheocast composite at normal loads of 9.8 N. All the samples show a pattern of grooves and ridges running parallel to each other in the sliding direction, caused by deformation and micro-ploughing of the soft alloy by the hard steel counter face. During wear, material is removed by delamination of layers, as depicted in marked region of Figure 9a, b. Figure 10 shows SEM micrographs of wear surfaces of alloy and composite tested at 29.4 N. At lower loads, the grooves produced are shallow as compared to higher loads. The worn surface of CG A356 alloy exhibits deep long grooves along the direction of sliding. Ploughing is a method for removing material from a surface by repeatedly pushing against the surface with a plough. Asperities on the surface cause friction and wear away the material.[38] The high magnification image (inset), showing the evidence of plough marks, indicates that the ploughing action predominately occurs in CG A356 alloy. The worn surface rheocast composite shows a wide range of terrains, including narrow grooves and almost flat surfaces. This is because TiB$_2$ particles restrict the flow of the metal when it is subjected to an applied load. Furthermore, the worn surface of composite materials has higher hardness than that of alloys, which makes it easier for the hard asperities of the counter face to be
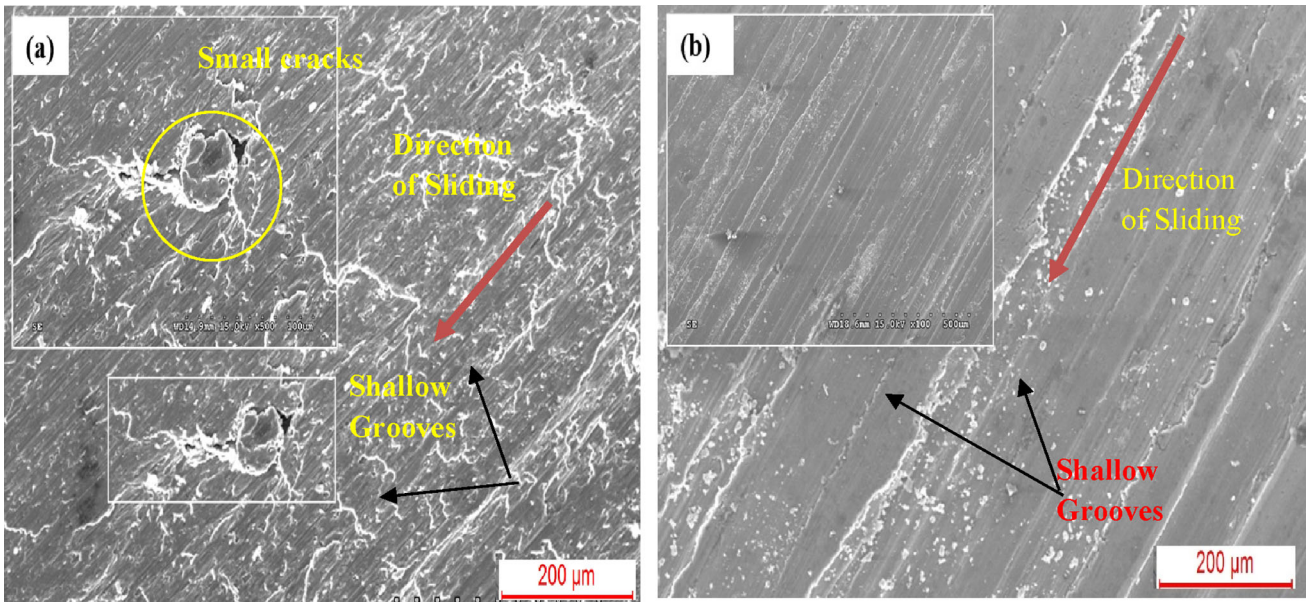
Figure 9. SEM micrograph showing wear surfaces at 9.8 N of (a) CG A356 alloy and (b) rheocast composite (inset high magnification).
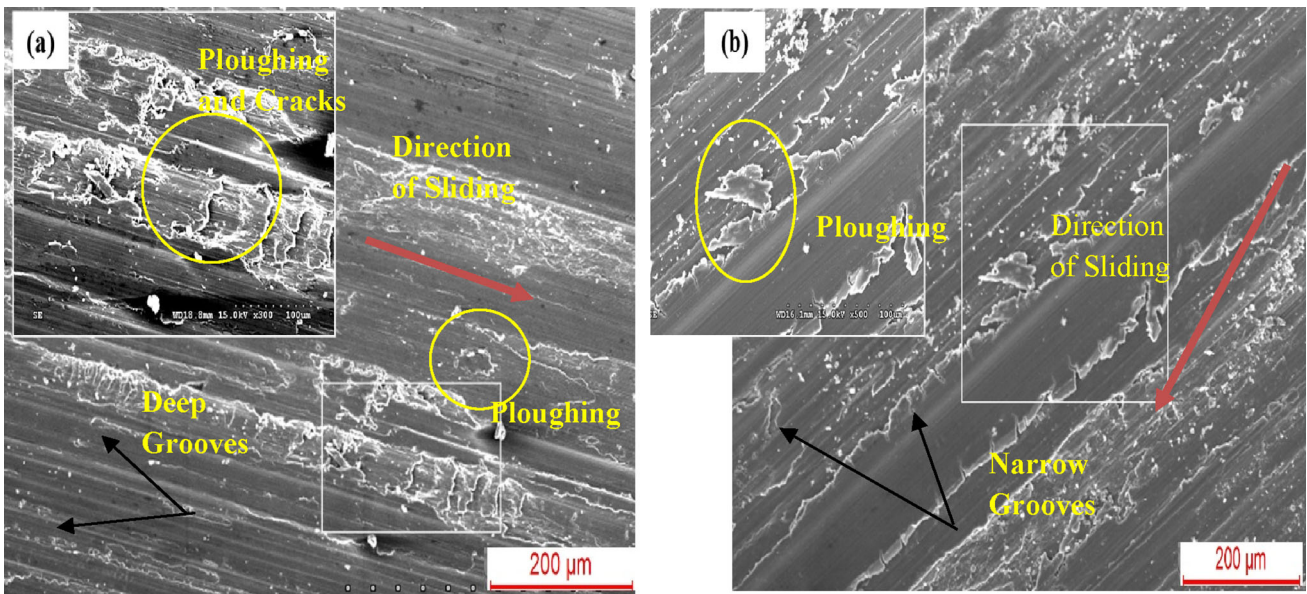

Figure 10. SEM micrograph showing wear surfaces at 29.4 N of (a) CG A356 alloy and (b) rheocast composite (inset high magnification).

removed during the polishing operation.[38] With an increase in load, the increase in wear loss can be attributed to the greater amount of deformation and damage.[38] The worn surface is partially oxidized during the wear test, and the presence of oxygen on the worn surface has been confirmed by EDS.

The EDS on wear debris of CG A356 alloy and rheocast composite tested at 9.8 N are shown in Figure 11a, b. Figure 12a and b shows the EDS of CG A356 alloy and rheocast composite wear debris tested at 29.4 N. The result shows the presence of Fe on both the alloy and composite specimen. It was found that the iron (Fe) content on worn surfaces increased with increasing applied loads. These results confirm the presence of a mechanical mixed layer formed between the wear surface and the counterface material.[39] The formation of iron-rich layers on the worn surfaces may also help reduce the wear rate of the composite materials.[38]

Surface Roughness

Roughness (Ra) of the worn surfaces was traced at specific locations and orientation using a contact type stylus profilometer at a load of 3 mg force and diameter (both in the
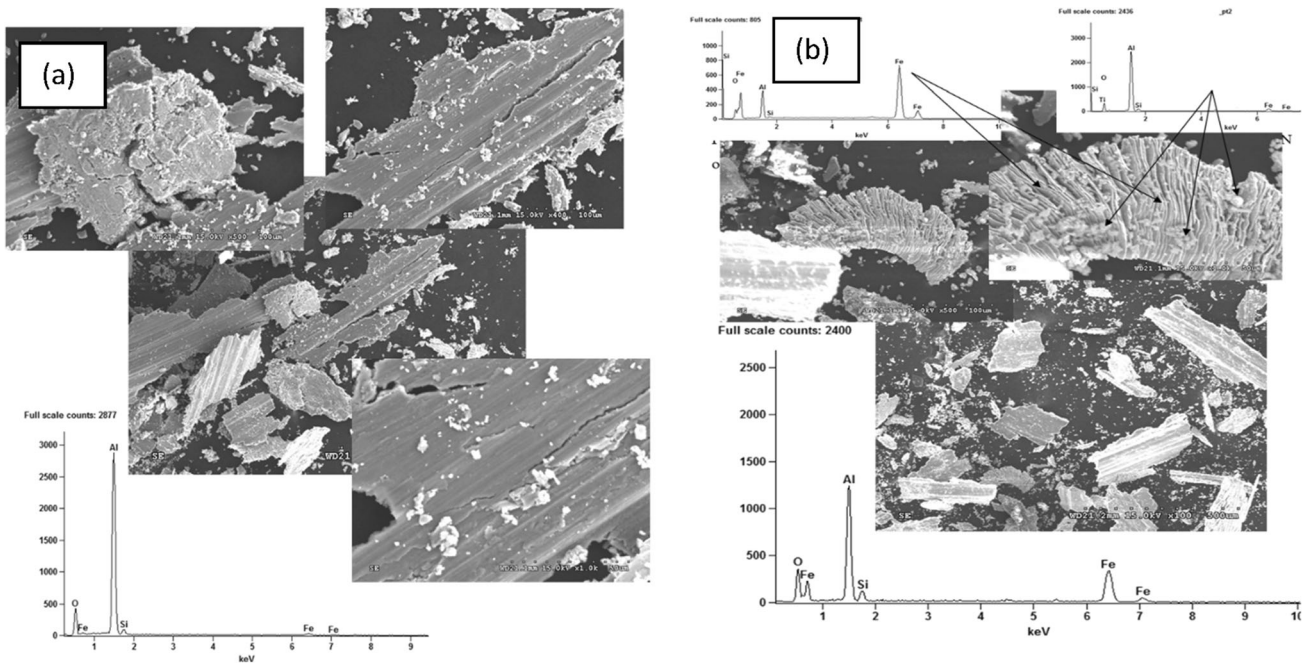
Figure 11. SEM images of wear debris generated on testing under a normal load of 9.8 N and EDS (a) CG A356 alloy (b) rheocast composite.
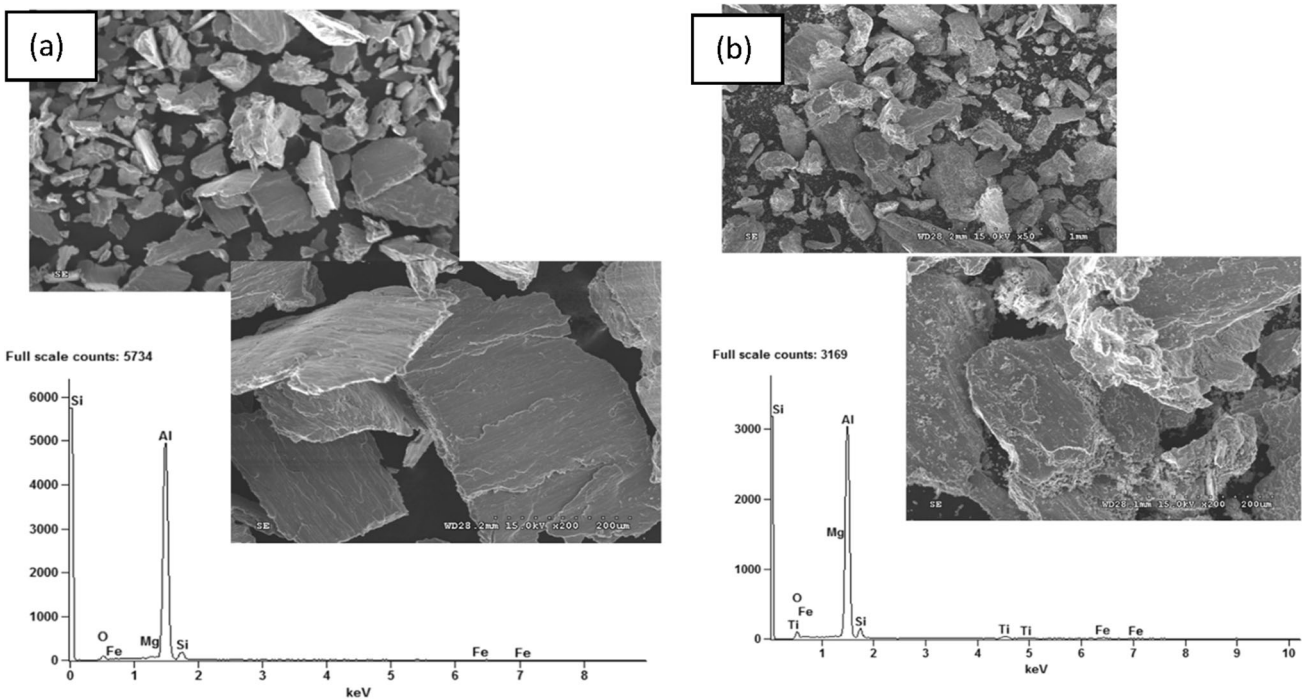

Figure 12. SEM images of wear debris generated on testing under a normal load of 29.4 N and EDS (a) CG A356 alloy (b) rheocast composite.

sliding and in the transverse direction). Figure 13 presents the two-dimensional (2D) profile of worn the surface of the CG A356 alloy and rheocast composite sample wear tested under a load of 29.4 N. The value of the Ra of the worn surface of CG A356 alloy is higher than that of rheocast composite. It may be noted that the surface roughness is directly proportional to the wear rates and inversely proportional to the hardness of investigated material.
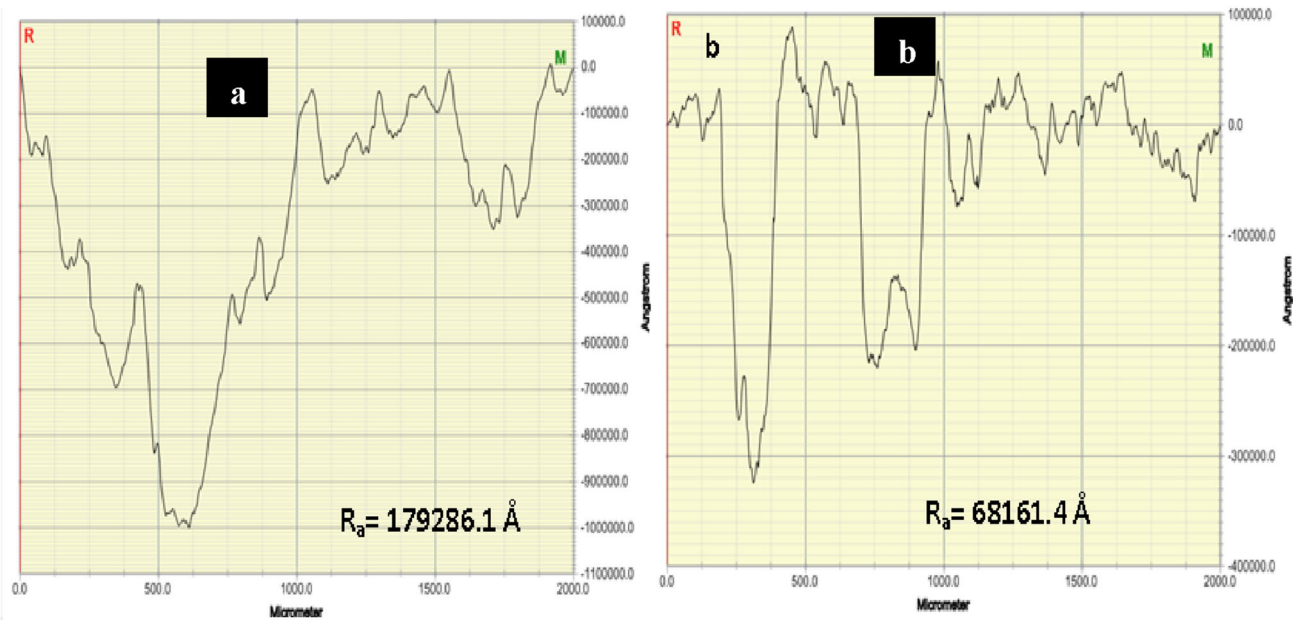
Figure 13. A typical view of the profile of the worn surface on the sample of (a) CGA356 and (b) rheocast composite.

Conclusions

In this work, A356/5% TiB_2 in situ composite was successfully fabricated by cooling slope process. The developed samples were subjected to mechanical, wear properties, and following conclusions were drawn from the investigation.

1. XRD analysis confirms the formation of TiB_2 particles and intermetallic phase Mg_2Si in the rheocast composite material.
2. The SEM micrograph shows the TiB_2 particles are mostly in the hexagonal or near spherical shape, with the size ranging from size 1 to 5 μm and uniformly distributed throughout the matrix. The presence of TiB_2 in the matrix enhanced the hardness and ultimate tensile strength properties except for elongation.
3. Optical microscopy, SEM and EDS analysis reveal that composite material exhibits morphology of primary phase nearly globular and rosette shapes and refined eutectic morphologies during the cooling slope process. This extent of variation in microstructure leads to change in observed mechanical properties.
4. The average values obtained are as follows: Young modulus, Yield strength, Tensile strength and elongation of rheocast composite are 77, 190, 225 and 7 %, respectively, which exhibit the best mechanical properties compared to of CG A356 aluminum alloy (Young modulus 70, Yield strength 170, Tensile strength 194 MPa and Elongation 9 %).
5. In the case of TiB_2 composite, a small amount of ploughing and cracking is present on the surface due to mild wear by abrasion and a smaller amount of plastic deformation of asperities, which is confirmed by SEM micrographs. Value of the Ra of the worn surface of rheocast composite is lower than the CG A356 alloy.

Acknowledgements

REFERENCES

1. G. Sigworth, Understanding quality in aluminum castings. Int. J. Met. (2011). https://doi.org/10.1007/BF03355504
2. G.K. Sigworth, T.A. Kuhn, Grain refinement of aluminum casting alloys. Int. J. Met. (2007). https://doi.org/10.1007/BF03355416
3. G.K. Sigworth, the modification of AI-SI casting alloys: important practical and theoretical aspects. Int. J. Met. (2008). https://doi.org/10.1007/BF033554251
4. V. Vembu, G. Ganesan, Heat treatment optimization for tensile properties of 8011 Al/15% SiCp metal matrix composite using response surface methodology. Def. Technol (2015). https://doi.org/10.1016/j.dt.2015.03.004

5. N. Nagaraj, K.V. Mahendra, M. Nagaral, Investigations on mechanical behaviour of micro graphite particulates reinforced Al-7Si alloy composites. in *IOP conference series: Mater. Sci. Eng.* (2018)

6. F. Akhlaghi, A. Lajevardi, H.M. Maghanaki, Effects of casting temperature on the microstructure and wear resistance of compocast A356/SiCp composites: a comparison between SS and SL routes. J. Mater. Process. Technol. (2004). https://doi.org/10.1016/j.jmatprotec.2004.04.328

7. H. Ghandvar, S. Farahany, M.H. Idris, Effect of wettability enhancement of SiC particles on impact toughness and dry sliding wear behavior of compocasted A356/20SiCp composites. Tribol. Trans. (2018). https://doi.org/10.1080/10402004.2016.1275902

8. W. Hoziefa, S. Toschi, M.M.Z. Ahmed, A. Morri, A.A. Mahdy, M.E.S. Seleman, A. Atlam, Influence of friction stir processing on the microstructure and mechanical properties of a compocast AA2024-Al$_2$O$_3$ nanocomposite. Mater. Des. (2016). https://doi.org/10.1016/j.matdes.2016.05.114

9. B.A. Kumar, N. Murugan, Metallurgical and mechanical characterization of stir cast AA6061-T6–AlNp composite. Mater. Des. (2012). https://doi.org/10.1016/j.matdes.2012.03.038

10. K. Kalaiselvan, N. Murugan, S. Parameswaran, Production and characterization of AA6061–B4C stir cast composite. Mater. Des. (2011). https://doi.org/10.1016/j.matdes.2011.03.018

11. C.S. Ramesh, R. Keshavamurthy, B.H. Channabasappa, A. Ahmed, Microstructure and mechanical properties of Ni–P coated Si$_3$N$_4$ reinforced Al6061 composites. Mater. Sci. Eng. A (2009). https://doi.org/10.1016/j.msea.2008.10.012

12. J.A.K. Gladston, N.M. Sheriff, I. Dinaharan, J.D. Raja Selvam, Production and characterization of rice husk ash particulate reinforced AA6061 aluminum alloy composites by compocasting. Trans. Nonferrous Met. Soc. China. (Engl. Edn.) (2015). https://doi.org/10.1016/S1003-6326(15)63653-6

13. J.D. Raja Selvam, D.S. Robinson Smart, I. Dinaharan, Microstructure and some mechanical properties of fly ash particulate reinforced AA6061 aluminum alloy composites prepared by compocasting. Mater. Des. (2013). https://doi.org/10.1016/j.matdes.2013.01.053

14. J.A.K. Gladston, I. Dinaharan, N.M. Sheriff, J.D.R. Selvam, Dry sliding wear behavior of AA6061 aluminum alloy composites reinforced rice husk ash particulates produced using compocasting. J. Asian. Cer. Soc. (2017). https://doi.org/10.1016/j.jascer.2017.03.005

15. S.K. Gautam, H. Roy, A.K. Lohar, S. Goutam, Effect of processing routes on structure-property correlationship of ADC 12 Al alloy. Mater. Res. Exp. (2019). https://doi.org/10.1088/2053-1591/aaec2c

16. M.S. Salleh, M.Z. Omar, J. Syarif, K.S. Alhawari, M.N. Mohammed, Microstructure and mechanical properties of thixoformed A319 aluminium alloy. Mater. des. (2014). https://doi.org/10.1016/j.matdes.2014.07.014

17. S.K. Gautam, H. Roy, A.K. Lohar, S.K. Samanta, G. Sutradhar, Microstructure characterization and mechanical properties of semi solid ADC 12 Al alloy. Int. J. Mod. Manuf. Technol. (2019). https://www.ijmmt.ro/vol11no12019/05_Sujeet_K_Gautam.pdf

18. S. Janudom, T. Rattanochaikul, R. Burapa, S. Wisutmethangoon, J. Wannasin, Feasibility of semi-solid die casting of ADC12 aluminum alloy. Trans. Nonferrous Met. Soc. China. (2010). https://doi.org/10.1016/S1003-6326(09)60370-8

19. J. Wannasin, S. Thanabumrungkul, Development of a semi-solid metal processing technique for aluminium casting applications. Songklanakarin J. Sci. Technol. (2008). https://www. thaiscience.info/journals/Article/SONG/10617714.pdf

20. M. Kiuchi, S. Sugiyama, A new process to manufacture semi-solid alloys. ISIJ Int. (1995). https://doi.org/10.2355/isijinternational.35.790

21. S. Ji, Z. Fan, M.J. Bevis, Semi-solid processing of engineering alloys by a twin-screw rheomoulding process. Mater. Sci. Eng. A. (2001). https://doi.org/10.1016/S0921-5093(00)01373-3

22. S. Ji, Z. Fan, Solidification behavior of Sn-15 wt pct Pb alloy under a high shear rate and high intensity of turbulence during semisolid processing. Metall. Mater. Trans. A. (2002). https://doi.org/10.1007/s11661-002-0338-4

23. S. Wang, F. Cao, R. Guan, J. Wen, Formation and evolution of non-dendritic microstructures of semisolid alloys prepared by shearing/cooling roll process. Cailiao Kexue Yu Jishu (J. Mater. Sci. Technol.) **22**(2), 195–199 (2006)

24. C. Vives, Electromagnetic refining of aluminum alloys by the CREM process: Part I. Working principle and metallurgical results. Metall. Mater. Trans. B. (1989). https://doi.org/10.1007/BF02655919

25. S.A. Alidokht, A. Abdollah-Zadeh, S. Soleymani, H. Assadi, Microstructure and tribological performance of an aluminum alloy based hybrid composite produced by friction stir processing. Mater. Des. (2011). https://doi.org/10.1016/j.matdes.2011.01.021

26. M.K. Akbari, H.R. Baharvandi, K. Shirvanimoghaddam, Tensile and fracture behavior of nano/micro TiB2 particle reinforced casting A356 aluminum alloy composites. Mater. Des. (2015). https://doi.org/10.1016/j.matdes.2014.10.048

27. C. Mallikarjuna, S.M. Shashidhara, U.S. Mallik, K.I. Parashivamurthy, Grain refinement and wear properties evaluation of aluminum alloy 2014 matrix-TiB$_2$ in-situ composites. Mater. Des. (2011). https://doi.org/10.1016/j.matdes.2011.01.036

28. P. Das, S.K. Samanta, R. Das, P. Dutta, Optimization of degree of sphericity of primary phase during

cooling slope casting of A356 Al alloy: Taguchi method and regression analysis. Measur (2014). https://doi.org/10.1016/j.measurement.2014.05.022

29. F. Chen, Z. Chen, F. Mao, T. Wang, Z. Cao, TiB₂reinforcedaluminum based in situ composites fabricated by stir casting. Mater. Sci. Eng. A. (2015). https://doi.org/10.1016/j.msea.2014.12.033

30. N. Saklakoğlu, S. Gencalp, Ş Kasman, İE. Saklakoğlu, Formation of globular microstructure in A380 aluminum alloy by cooling slope casting. Advan. Mat. Res. Trans. Tech. **264**, 272–277 (2011)

31. S.K. Gautam, N. Mandal, H. Roy, A.K. Lohar, S.K. Samanat, S. Goutam, Optimization of processing parameters of cooling slope process for semi-solid casting of ADC 12 Al. J. Brazil Soc. Mech. Sci. Eng. (2018). https://doi.org/10.1007/s40430-018-1213-6

32. A.K. Yadav, V. Kumar, S. Mohan, Microstructure and mechanical properties of an in situ Al 356-Mg2Si-TiB2 hybrid composite prepared by stir and cooling slope casting. Int. J. Met. (2022). https://doi.org/10.1007/s40962-022-00804-x

33. S. Saffari, F. Akhlaghi, Microstructure and mechanical properties of Al-Mg₂Si composite fabricated in-situ by vibrating cooling slope. Trans. Nonferrous Met. Soc. China. (2018). https://doi.org/10.1016/S1003-6326(18)64693-X

34. M.C. Mehta, D. Mandal, S.K. Chaudhury, Microstructural changes and quality improvement of Al7Si02Mg (356) alloy by die vibration. Int. J. Met. (2020). https://doi.org/10.1007/s40962-020-00408-3

35. T. Wang, Z. Chen, Y. Zheng, Y. Zhao, H. Kang, L. Gao, Development of TiB₂ reinforced aluminum foundry alloy based in situ composites–Part II: Enhancing the practical aluminum foundry alloys using the improved Al–5 wt% TiB₂ master composite upon dilution. Mater. Sci. Eng. A. (2014). https://doi.org/10.1016/j.msea.2014.03.021

36. Z. Chen, T. Wang, Y. Zheng, Y. Zhao, H. Kang, L. Gao, Development of TiB₂ reinforced aluminum foundry alloy based in situ composites–Part I: An improved halide salt route to fabricate Al–5 wt% TiB₂ master composite. Mater. Sci. Eng. A. (2014). https://doi.org/10.1016/j.msea.2014.02.088

37. A. Changizi, A. Kalkanli, N. Sevinc, Production of in situ aluminum–titanium diboride master alloy formed by slag–metal reaction. J. Alloys Compd. (2011). https://doi.org/10.1016/j.jallcom.2010.08.089

38. S. Suresh, N.S.V. Moorthi, S.C. Vettivel, N. Selvakumar, Mechanical behavior and wear prediction of stir cast Al–TiB₂ composites using response surface methodology. Mater. Des. (2014). https://doi.org/10.1016/j.matdes.2014.02.053

39. S. Kumar, M. Chakraborty, V.S. Sarma, B.S. Murty, Tensile and wear behaviour of in situ Al–7Si/TiB₂ particulate composites. Wear (2008). https://doi.org/10.1016/j.wear.2007.09.007